



# Parametric removal rate survey study and numerical modeling for deterministic optics manufacturing

VIPENDER SINGH NEGI,<sup>1,2,\*</sup>  HARRY GARG,<sup>1,2</sup> SHRAVAN KUMAR RR,<sup>2</sup> VINOD KARAR,<sup>2</sup> UMESH KUMAR TIWARI,<sup>1,2</sup> AND DAE WOOK KIM<sup>3,4</sup>

<sup>1</sup>Academy of Scientific and Innovative Research (AcSIR), Council of Scientific and Industrial Research-Central Scientific Instruments Organisation (CSIR-CSIO) Campus, Chandigarh 160030, India

<sup>2</sup>Council of Scientific and Industrial Research-Central Scientific Instruments Organisation (CSIR-CSIO), Chandigarh 160030, India

<sup>3</sup>James C. Wyant College of Optical Sciences, The University of Arizona, Tucson, AZ 85721, USA

<sup>4</sup>Department of Astronomy and Steward Observatory, The University of Arizona, Tucson, AZ 85721, USA  
\*vipender@live.com

**Abstract:** Surface errors directly affect the performance of optical systems in terms of contrast and resolution. Surface figure errors at different surface scales are deterministically removed using controlled material removal rate (*MRR*) during a precision optics fabrication process. We systematically sectioned the wide range of *MRR* space with systematic parameters and experimentally evaluated and mapped the *MRR* values using a flexible membrane-polishing tool. We performed numerical analysis with a tool influence function model using a distributed *MRR*-based Preston's constant evaluation approach. The analysis procedure was applied to a series of experimental data along with the tool influence function models to evaluate removal rates. In order to provide referenceable survey data without entangled information, we designed the experiments using Taguchi's L27 orthogonal array involving five control parameters and statistically analyzed a large number of programmatic experiments. The analysis of variance showed that the most significant parameters for achieving a higher *MRR* are the spot size and active diameter.

© 2020 Optical Society of America under the terms of the [OSA Open Access Publishing Agreement](#)

## 1. Introduction

Polishing is the final stage of optical surfacing in the production chain of modern optical components. It is the most critical finishing process in the fabrication of high-quality optics. However, there is limited process certainty concerning the reproducibility of surface quality. Therefore, attempts have been made to optimize the polishing process [1–3]. In recent years, the requirements for high-performance optics have increased, processes have advanced, and new fabrication and finishing methods have been developed. This growth is also motivated by the increasing demand to manufacture complex aspheric and free-form surfaces. The full potential of the advanced methods for fabricating optics is yet to be realized.

Computer-controlled optical surfacing (CCOS) of aspheric and free-form optical surfaces requires a sequence of polishing processes using different tools. The process starts with the pre-polishing of a fine ground surface to remove sub-surface damage and reduce surface roughness [4,5]. This stage is followed by correction polishing to control the low spatial frequency figure, but this process leaves mid-to-high spatial frequency residual surface errors [6]. Therefore, monitoring and minimizing these errors are important in precision optical system manufacturing. These surface errors and scattering phenomena due to surface roughness reduce the contrast and resolution of optical systems. In particular, systems used in short-wavelength applications are

often directly affected as the total integrated scatter is inversely proportional to the square of the system wavelength [7,8].

These errors are difficult to control using CCOS, as the minimum usable polishing contact size is often higher than the mid-to-high spatial frequency range of surface errors. Researchers have attempted to avoid or remove these errors using methods such as random paths, orbital tool motion, full-size pitch polishing, and fluid jet polishing [9–12]. Surface errors are estimated quantitatively by determining the root mean square (rms) of surface errors over a range of frequencies; further, the power spectral density is considered as a function of the spatial frequency, and the bidirectional reflectance distribution function is used for scattering measurement merit [13,14].

Polishing experiments using modified tools and different process parameters to control the figure and finish have been reported [11,15–19]. Also, the bonnet tool removal process has been investigated and analyzed adopting detailed micro-scale analysis model for the material removal mechanisms [20–21]. Most studies have focused on modifying existing tools, optimizing the tool speed, analyzing removal characteristics, observing figure change during polishing of free-form optics, and evaluating the effect of pad wear on the polishing process. There are various fabrication and process optimization approaches for guiding different polishing processes to produce specific components. Especially, *MRR*, which is the most fundamental and critical property, is affected by many uncontrollable random factors. For large astronomical mirror (e.g., 4 - 8 m class mirrors) fabrication applications, it is often not practical to control some parameters (ambient temperature, slurry particle size and distribution) due to the large volume of the environment and practical/cost limitations. It is difficult to perform objective comparisons between the results of separately reported experiments. Although previous studies attempted to clarify the *MRR* during polishing using theoretical modeling and experimental analyses [22–27], deterministic and fully valid relationships are yet to be established for estimating the *MRR*. Moreover, findings from different studies cannot be generalized owing to differences in the process setups used in the studies.

The invaluable, yet fragmented and separately investigated, collection of removal rates can be further improved and refined to provide referenceable *MRR* data through re-investigating their material removal rates (*MRRs*) under a carefully designed single large campaign. Such a focused parametric experimental survey guarantees uniformly controlled fabrication conditions and compatible *MRR* space mapping between data points. During our parametric experimental survey, volumetric analysis was performed to determine *MRRs* under dynamic conditions, considering configuration-specific factors such as the actual tool size, stroke motion, stroke speed, and polishing pressure. Hence, this study aims to address the gap between various experimental *MRR* data and identify the most critical parameters that can be used to control the sub-aperture pad polishing process.

We performed numerical and experimental analyses of *MRRs* during flexible membrane polishing; numerical results were validated through systematically controlled and calibrated experimental observations. The tool influence function (TIF) was applied to model and take account of the effects of the relative velocity and tool inclination on the *MRR*. Simulated dynamic *MRRs* were analyzed for different workpiece and tool speeds. The process parameters considered in the analysis were the active diameter, feed, pressure, spot size, and tool speed. This paper clearly outlines our approach to evaluate the constant coefficient in Preston's equation through distributed *MRR*-based analysis of the TIF. In order to serve the community as a reference, by following the identical procedure and modeling process, all the experimental data can be reproduced and verified independently. Also, the simulated and measured TIFs are nearly the same; therefore, the proposed method to evaluate the constant-coefficient can be used efficiently for controlling the sub-aperture polishing process and fabricating precision optical lenses.

This paper is organized as follows. Section 2 gives a brief overview of the membrane-polishing tool configuration used for the experiments and the concept of *MRR*. A distributed *MRR*-based method to evaluate Preston's constant is outlined in Section 3. In Section 4, the parametric survey result of the *MRR* study is analyzed and presented. The conclusion is summarized in Section 5.

## 2. Experiment setup and material removal rate

### 2.1. Sub-aperture membrane-polishing tool set-up

The aspherical experiment samples were polished using a flexible membrane-polishing tool (MCP 250, OptoTech, Article number 185-90-1000). Figure 1 shows the axis configuration of the polishing machine, the polishing tool and workpiece, and the kinematic relationship between the tool and workpiece. For polishing, the workpiece and tool were rotated at a predetermined speed along their axes. The contact spot was formed by compressing an inflated tool against the workpiece. Also, the active diameter  $A$ , which affects the velocity field in the contact area, is defined as shown in Fig. 1(c). Thereafter, the polishing tool moved radially following the workpiece curvature from the center to the outer edge of the sample.

### 2.2. Mathematical *MRR* model

Most precision glass polishing is performed using loose abrasives in the form of a suspension and it is usually the final manufacturing process in optical component fabrication. Mechanical and chemical interactions during glass polishing lead to smoothing of the surface [28–33]. The ablation, flow, chemical, and wear-friction hypotheses describe the physical changes that occur at the glass boundary during polishing. The model explaining the *MRR* during glass polishing is based on Preston's equation [28]. It states that the rate of material removal during a glass polishing is proportional to the contact pressure and relative velocity between the tool and the workpiece. This is expressed as

$$\frac{dz(x,y)}{dt} = -kp(x,y)v_{tw}(x,y), \quad (1)$$

where  $dz/dt$  is the removal depth per unit time,  $k$  is Preston's constant,  $p(x,y)$  is the pressure, and  $v_{tw}(x,y)$  is the relative velocity between the tool and workpiece. Thus, a prerequisite for modeling is defining the relative velocity and contact pressure. Here, tool kinematics are obtained by considering the tool geometry, workpiece geometry, tool radius, tool inclination, tool compression, workpiece speed, and tool speed.

Spatial distribution of material removal is often controlled using the dwell time as a function of tool position on the optic under fabrication. Dwell time is the time required to remove the local surface error and it is proportional to the surface error magnitude. The removal depth  $z(x,y)$  and depth removal rate  $DRR(x,y)$  at any arbitrary contact point are given by

$$z(x,y) = -\int_0^\tau kp(x,y)v_{tw}(x,y)dt, \quad (2)$$

$$DRR(x,y) = -\frac{1}{\tau} \int_0^\tau kp(x,y)v_{tw}(x,y)dt, \quad (3)$$

where  $\tau$  is the dwell time at an arbitrary point  $(x,y)$ .

During the polishing process, the inflated tool rotates and moves on the workpiece. Both the tool and workpiece motion influences the *MRR* according to the tool position on the workpiece surface. Figure 1(c) shows the tool inclination angle ( $\phi$ ), position of the tool center ( $\mathbf{r}_c$ ), position vector ( $\mathbf{r}_p$ ) of the arbitrary contact point, and displacement vector ( $\mathbf{r}_{pc}$ ) of the arbitrary point with

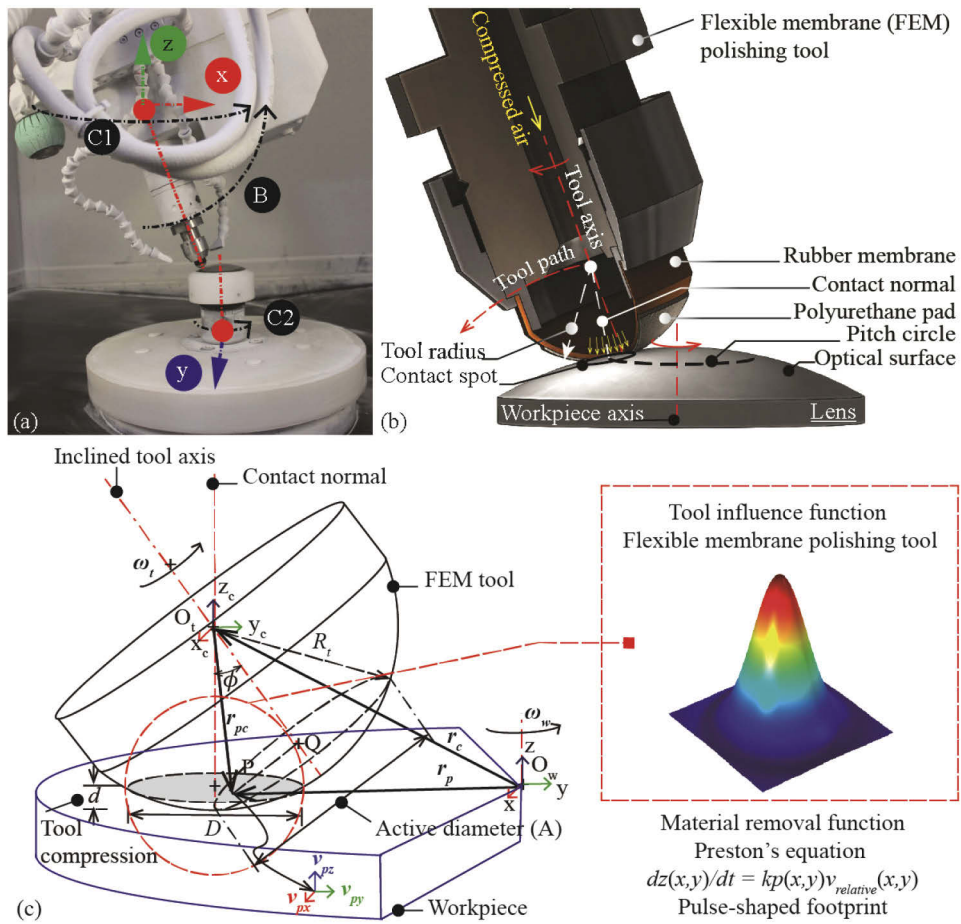


**Fig. 1.** (a) The material removal rate experiment setup using the machine tool (MCP 250, OptoTech) with linear x, y, and z axes, and rotational B, C1, and C2 axes. (b) Contact between sub-aperture flexible membrane-polishing tool and the workpiece during polishing. (c) Representative diagram of the workpiece and tool parameters, along with the material removal function of the flexible membrane-polishing tool.

respect to the tool center, which are given by

$$\mathbf{r}_c = \{x_c, y_c, z_c\}, \mathbf{r}_p = \{x, y, z\}, \quad (4)$$

$$\mathbf{r}_{pc} = \mathbf{r}_p - \mathbf{r}_c. \quad (5)$$

The respective angular velocities of the tool and workpiece, namely  $\boldsymbol{\omega}_t$  and  $\boldsymbol{\omega}_w$ , are given by

$$\boldsymbol{\omega}_t = 2\pi N_t \{1, -\sin(\phi), \cos(\phi)\}, \quad (6)$$

$$\boldsymbol{\omega}_w = 2\pi N_w \{0, 0, 1\}, \quad (7)$$

where  $N_t$  is the rotational speed of the tool (rpm) and  $N_w$  is that of the workpiece. The respective tangential velocities of the tool and workpiece are

$$\mathbf{v}_t = \boldsymbol{\omega}_t \times \mathbf{r}_{pc}, \quad (8)$$

$$\mathbf{v}_w = \boldsymbol{\omega}_w \times \mathbf{r}_p. \quad (9)$$

The relative velocity of the tool with respect to the workpiece, where  $\mathbf{v}_f = (v_{fx}, v_{fy}, v_{fz})$  is the tool feed velocity, is given by

$$\mathbf{v}_{tw} = \mathbf{v}_t + \mathbf{v}_f + (-\mathbf{v}_w), \quad (10)$$

$$\mathbf{v}_{tw} = \boldsymbol{\omega}_t \times (\mathbf{r}_p - \mathbf{r}_c) + \mathbf{v}_f - \boldsymbol{\omega}_w \times \mathbf{r}_p. \quad (11)$$

Contact pressure distribution is obtained by assuming that the pressure is distributed in a Gaussian form. The pressure at the arbitrary contact point is given by

$$p(x, y) = p_0 e^{\left(-\frac{1}{2} \frac{(x-x_c)^2 + (y-y_c)^2}{\sigma^2}\right)}, \quad (12)$$

where  $p_0$  is the peak pressure and  $\sigma$  is a constant.

It is better to have rotationally symmetric removal function with the peak at the center e.g. bell shaped or Gaussian-like removal function. The convolution of such smooth symmetric removal function is identical in every direction, so the dwell time evaluation and optimization become simple. It is worth to note that, if the tool offset is too big, flexible membrane polishing tool may warp and the removal shape is deviating from the Gaussian-like profile. In the presented study the offset/compression of the tool was kept within the limit preventing the warping phenomena.

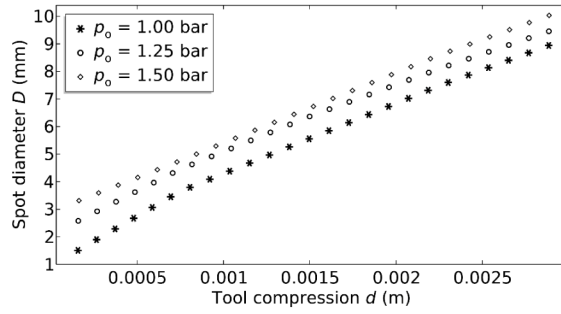
Transformation of the removal function over the workpiece surface for tool motion was carried by evaluating Gaussian exponent about the tool contact center. Also, the removal function is set to be zero at  $D/2$  with respect to tool center over the workpiece. Here the constant  $\sigma$  defines the standard deviation (i.e., spatial size) of the Gaussian-like removal function which is fraction of contact diameter.

Figure 2 shows the change in spot size with tool compression for different pressure 1, 1.25 and 5 bar. Static finite element analysis model was applied to study the effect of contact pressure on spot diameter during contact between flexible membrane polishing tool and workpiece. The Mooney-Rivlin method [29] was used to study the interaction between spot size and pressure.

The *MRR* is defined using Eqs. (1), (11), and (12) as follows:

$$MRR = -\frac{kp_0}{\tau} \int_0^\tau \left( \iint e^{\left(-\frac{1}{2} \frac{(x-x_c)^2 + (y-y_c)^2}{\sigma^2}\right)} v_{tw}(x, y) dx dy \right) dt. \quad (13)$$

The domain constraint for *MRR* evaluation is given by  $\sqrt{((x - x_c)^2 + (y - y_c)^2)} \leq \frac{D}{2}$ , where  $D$  is the spot diameter.



**Fig. 2.** Spot diameter ( $D$ ) for different tool compressions ( $d$ ) at pressure 1, 1.25 and 1.5 bar for aspherical surface used in the parametric survey study in Section 4.

### 3. Comprehensive distributed *MRR*-based modeling and evaluation

#### 3.1. *MRR* evaluation using distributed *MRR*-based approach

A common method to estimate Preston's coefficient is using the ratio of the depth removal rate to the product of the peak pressure and velocity. However, physical parameters (e.g., elastic recovery, plastic removal, and brittle cracking) [34] across the contact surface may vary along the radial direction during actual polishing runs. Therefore, the Preston's constant needs to be measured considering the distributed effect of removal depth, pressure and velocity in contact area as

$$k_{dist} = \frac{1}{\tau} \left| \frac{\iint \frac{z(x,y)}{p(x,y)v_{tw}(x,y)} dx dy}{\iint dx dy} \right| = \frac{4}{\pi D^2 \tau} \left| \iint \frac{z(x,y)}{p(x,y)v_{tw}(x,y)} dx dy \right|, \quad (14)$$

where  $k_{dist}$  is the Preston's constant obtained using distributed *MRR*-based method. As shown in Eq. (14), the volume of the TIF is used to obtain the constant in Preston's equation.

The newly defined  $k_{dist}$  Eq. (14) is different from the two traditional evaluation methods, the peak-to-valley based  $k_p$  [35] evaluation approach in Eq. (15) and the volume-based  $k_V$  [11] method in Eq. (16).

$$k_p = \frac{1}{\tau} \left| \frac{z(x,y)_{\max}}{(p(x,y)v_{tw})_{\max}} \right| \quad (15)$$

$$k_V = \left| \frac{\text{Volume}}{\int_0^\tau \left( \iint (p(x,y)v_{tw}(x,y)) dx dy \right) dt} \right| \quad (16)$$

Also, the  $k_{dist}$  is directly related to the *MRR* and *DRR* as Eqs. (17) and (18), which can be precisely measured from actual measurements. The measured *MRR* can be used to calculate the  $k_{dist}$ . The improved performance of  $k_{dist}$  compared to the two traditional methods will be investigated and discussed in Section 4.1. The measured *MRR* library data from the parametric survey experiment are presented in Section 4.4 with the calculated  $k_{dist}$  values.

The average depth removal rate (*DRR*) using Eqs. (3), (11), (12), and (14) for a dwell time  $\tau$  is

$$DRR(x,y) = -\frac{k_{dist} p_0}{\tau} \int_0^\tau e^{\left(-\frac{1}{2} \frac{(x-x_c)^2 + (y-y_c)^2}{\sigma^2}\right)} v_{tw}(x,y) dt. \quad (17)$$

Finally, the *MRR* is obtained through areal integration of the *DRR*.

$$MRR = -\frac{k_{dist} p_0}{\tau} \int_0^\tau \left( \iint e^{\left(-\frac{1}{2} \frac{(x-x_c)^2 + (y-y_c)^2}{\sigma^2}\right)} v_{tw}(x,y) dx dy \right) dt \quad (18)$$

To assess the experimental volume of material removed during polishing experiments, the cross-section of the polished glass surface was measured across the diameter using two profilometers (MarForm MFU 200 Asphere 3D, Mahr and Talysurf PGI 120, Taylor Hobson). The difference between the successive profile measurements before and after the polishing run measures the amount of material removed during polishing. The average *MRR* was calculated as the ratio of the volume of material removed to the polishing process time (i.e., 2047, 1638, and 1365 s, which corresponds to feed rates of 0.8, 1, and 1.2 mm/min as defined in the experiments); a mean diameter of 54 mm was set for polishing. Profile deviation measurements were performed within the entire polishing zone shown in Fig. 3.

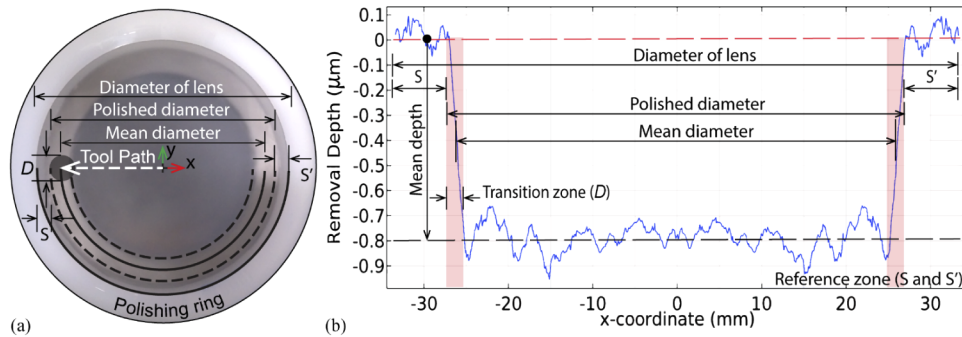


**Fig. 3.** (a) An example workpiece surface with a polishing ring used in the survey study and (b) its measured removal profile obtained along the workpiece diameter to evaluate experimental *MRR*.

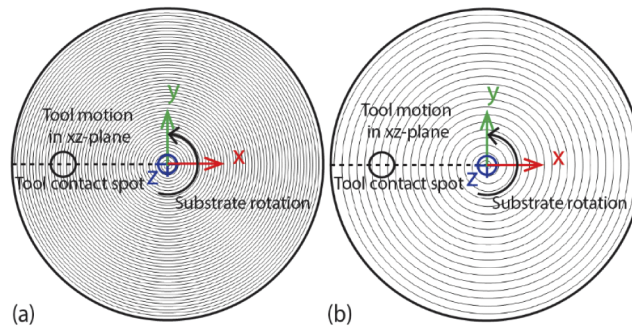
The complete polishing zone is the sum of the area within the ring defined by the mean diameter and spot size; the remaining outer ring is the reference for differential evaluation. All samples were polished at a constant workpiece rotation speed (780 rpm) and different tool speeds, according to the experimental conditions. Figure 3(b) shows an example of a differential profile (i.e., removal profile) obtained from the polishing run.

### 3.2. Relative velocity modeling at the interface

Sub-aperture optical polishing of symmetric surfaces can be performed in two ways: 1) using the workpiece axis as a spindle and 2) using the workpiece axis as an additional rotational axis as shown in Fig. 4. Using the workpiece axis as a spindle has the advantage of allowing the process to operate at a relatively high velocity; therefore, the low-to-high spatial frequency error may be avoided using an optimized radial feed function. When the workpiece axis acts as a rotational axis, the process operates at a low relative velocity. Table 1 lists the process parameters used in the relative velocity simulation and analysis.

**Table 1. Process parameters for relative velocity simulation and analysis.**

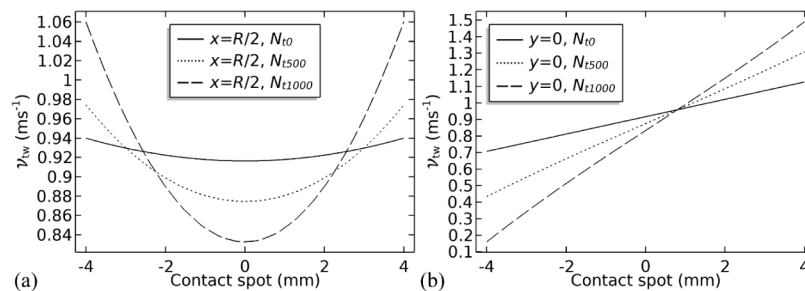
Parameter	Value
Workpiece diameter ( $D_w$ )	70 mm
Pressure ( $p_o$ )	1 bar
Workpiece speed ( $N_w$ )	-500 rpm
Tool speed ( $N_t$ )	0, 500, and 1,000 rpm
Tool inclination angle ( $\phi$ )	5°
Tool radius ( $R_t$ )	10 mm



**Fig. 4.** Schematic spiral tool path diagrams comparing (a) constant high-speed substrate rotation case and (b) controllable lower speed rotation case.

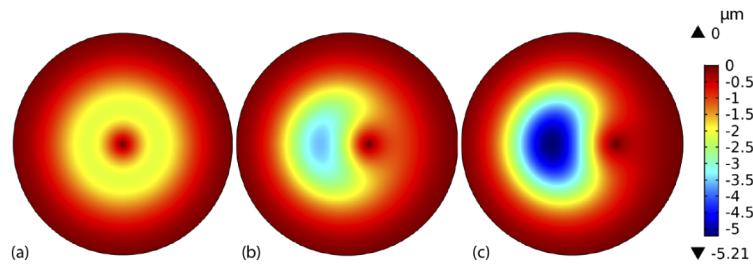
To fully explore and represent the wide range of possible variation of tool speed relative to workpiece speed, the tool speed was kept equal or double the workpiece speed. However, for actual applications, any variations of the tool speed within the explored range may reduce repeating errors.

Figure 5 shows the relative velocity along two sections of the contact spot. Figure 5(a) shows the section of the spot along section line  $x = R/2$ , where  $R = D_w/2$ . As this line is along the plane perpendicular to the tool inclination plane, the velocity profile is symmetric. A change in the velocity distribution profile can be observed where there is an increase in the difference between the tool velocities at the tool edge and center. This clearly shows the variation in the tool velocity along the radial direction. Here, the effect of the workpiece speed is greater than that of the tool speed. Sectional velocity profiles shown in Fig. 5(b) are evaluated along the section line  $y = 0$ , at the spot center coordinate of  $(R/2, 0)$ . The negative coordinate indicates points towards workpiece center and the positive points are towards the edge of the workpiece. Difference between the relative velocity across the two ends is increasing as we increase the tool velocity.



**Fig. 5.** Model simulation of the relative velocities in the tool-workpiece contact region for three tool speed  $N_t$  (in rpm) cases: (a) profile at section  $x = R/2$  and (b) profile at section  $y = 0$ .

Also, the effect of tool inclination on the  $MRR$  was modeled assuming a flexible membrane tool (radius  $R_t = 10$  mm). The removal depth was evaluated at a tool speed  $N_t = 500$  rpm, pressure  $p_o = 1$  bar, spot diameter  $D = 8$  mm, workpiece speed  $N_w = 0$  rpm, and time  $\tau = 2$  min. Figure 6 shows the change in the material removal depth and shape of the removal function for  $\phi = 0, 5,$  and  $10^\circ$ . The  $MRR$  increased with tool inclination; the calculated  $MRR$ s for  $\phi = 0, 5,$  and  $10^\circ$  were  $0.0204, 0.0223,$  and  $0.0270$   $\text{mm}^3/\text{min}$ , respectively.



**Fig. 6.** Simulated removal depth contour maps (m) at  $N_t = 500$  rpm, pressure  $p_o = 1$  bar,  $D = 8$  mm,  $N_w = 0$  rpm, and time  $\tau = 120$  s for each radial position. (a)  $\phi = 0$ , (b)  $\phi = 5$ , and (c)  $\phi = 10^\circ$ .

### 3.3. Numerical study of Instantaneous DRR and MRR

The modeled *DRR* was numerically evaluated using Preston's equation. Figure 7 shows the influence of the workpiece speed on the instantaneous *DRR* under the following process conditions:  $N_t = 500$  rpm, pressure  $p_o = 1$  bar,  $D = 8$  mm, and tool center on  $x$ -axis at  $x = R/2$  for  $N_w = 0, 250$ , and  $750$  rpm. Figure 7(a) shows a low *DRR* with velocity contour lines that are more circular and concentric (i.e., non-uniform) toward the tool rotation axis. The velocity contour lines in Fig. 7(b) are curved and centered about the workpiece rotation axis. Figure 7(c) shows the velocity contour lines have less curvature and are more uniformly distributed, so the *DRR* shows a Gaussian-like distribution. In other words, at a low workpiece rotation speed compared to the tool rotation speed, the influence that the tool motion has on the *DRR* distribution is asymmetric and depends on the tool parameters and its inclination. An increase in workpiece speed can result in a more uniform velocity distribution like the case in Fig. 7(c). The influence of the workpiece rotation and the tool's pressure distribution dominates the *DRR* shape and distribution of material removal in the contact zone.

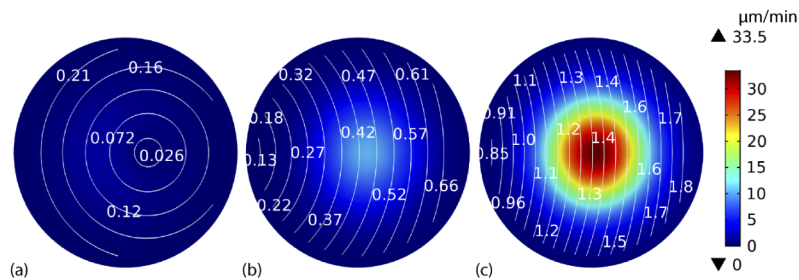


**Fig. 7.** Instantaneous depth removal rate (*DRR*) at  $N_t = 500$  rpm,  $p_o = 1$  bar, and tool center on  $x$ -axis at  $x = R/2$  for (a)  $N_w = 0$ , (b)  $250$ , and (c)  $750$  rpm. The white contour lines represent the relative velocity between the tool and workpiece (in m/s).

To study the effect that the workpiece and tool speeds have on *MRR*, two case studies were performed for each 6 minutes run with different workpiece and tool speed combinations. A linear feed was provided for radial travel of 35 mm with a lead-in distance of 4 mm from the edge to the center of the workpiece. For the first case study, Fig. 8(a) shows the variation in the *MRR* change along the radial position for  $N_w = 250, 500, 750$ , and  $1,000$  rpm (with  $N_t = 500$  rpm, pressure  $p_o = 1$  bar,  $\phi = 5^\circ$ ,  $D = 8$  mm). Increasing the workpiece speed significantly increases the *MRR* from the center to the edge. Another set of conditions was examined as the second case, in which the workpiece speed was kept constant while the tool speed was varied for  $N_t = 250, 500, 750$ , and  $1,000$  rpm (with  $N_w = 500$  rpm, pressure  $p_o = 1$  bar,  $\phi = 5^\circ$ ,  $D = 8$  mm) as shown

in Fig. 8(b). A comparison of Figs. 8(a) and (b) shows that increasing the workpiece speed significantly impacts the  $MRR$  along the radial direction compared to the result of increasing the tool speed case. Increasing the difference between workpiece and tool speed increases (or decreases) the relative velocity at the center causing excessive (or less) removal at the center. However, the overall material removal rate mainly depends on the workpiece speed. This needs to be carefully considered during the CCOS simulation and optimization process.

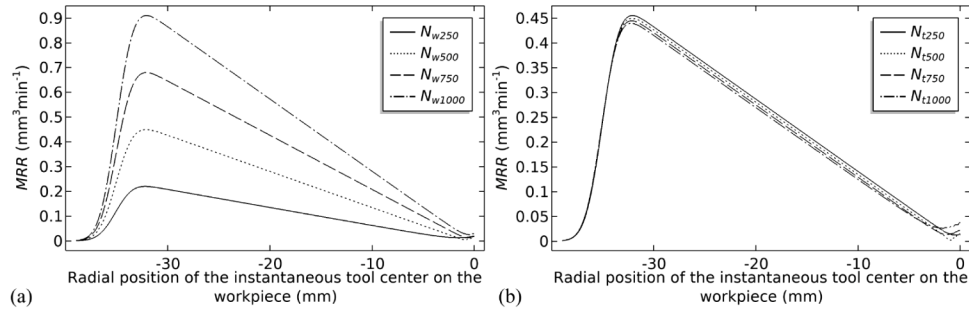


**Fig. 8.** The  $MRR$  variation along the instantaneous radial position of the tool center on a rotating workpiece. (a)  $N_t = 500$  rpm, pressure of  $p_o = 1$  bar,  $\phi = 5^\circ$ , and  $D = 8$  mm for  $N_w = 250, 500, 750$ , and  $1,000$  rpm. (b)  $N_w = 500$  rpm, pressure of  $p_o = 1$  bar,  $\phi = 5^\circ$ , and  $D = 8$  mm for  $N_t = 250, 500, 750$ , and  $1,000$  rpm.

## 4. Parametric survey experiments of $MRR$

### 4.1. Experimental verification of the numerical $MRR$ model

Before conducting the  $MRR$  survey study, experimental verification of the  $MRR$  modeling and evaluation (Section 3) was performed on BK7 optical glass (workpiece diameter of 70 mm). The finely ground surface was polished before obtaining the shape of the removal zone in order to avoid overestimated removal measurements due to the non-uniform initial surface height distribution. The workpiece was kept stationary during polishing. The tool (radius  $R_t = 10$  mm; pressure  $p_o = 1$  bar) was pressed against the workpiece, creating a compression spot with a diameter of 9.2 mm. The tool was inclined at  $5^\circ$  to the contact normal and operated for 2 minutes. Figure 9 shows the images of polished zone, measured topography, and simulated topography, respectively.

An experimental peak material removal depth of 3.66  $\mu\text{m}$  was measured using profilometry. The simulation was performed and compared as shown in Fig. 9(c). A peak removal depth of 3.82  $\mu\text{m}$  was obtained for the removal zone. To measure the polished contact spot, the tilt on the workpiece was removed using the measurement system. For the evaluation, the reference measurement zone was set to  $z = 0$ . Figure 9(c) shows the pressure contour lines and relative velocity field. The velocity is reduced near the tooltip, and it is relatively higher on the opposite side. The resulting tool influence function produces an approximate bean shape.

The  $MRR$  and  $DRR$  were evaluated using the distributed  $MRR$ -based process described in Section 2 and 3. This approach is more stable than those obtained with a traditional single-point (e.g., peak) evaluation method where a peak-removal depth may not reflect the overall characteristic of actual removal footprint. Also, this is a good alternative or cross-check solution for a non-trivial TIF evaluation case where a common volume-based calculation (i.e., using the total volume within a pre-defined TIF boundary) may have practical uncertainties due to the noisy low removal areas and ambiguous actual effective spot size estimation. The actual data processing steps applying the distributed  $MRR$ -based calculation is depicted in Fig. 10. Comparison with the other traditional methods is also carried and provided as a benchmark.

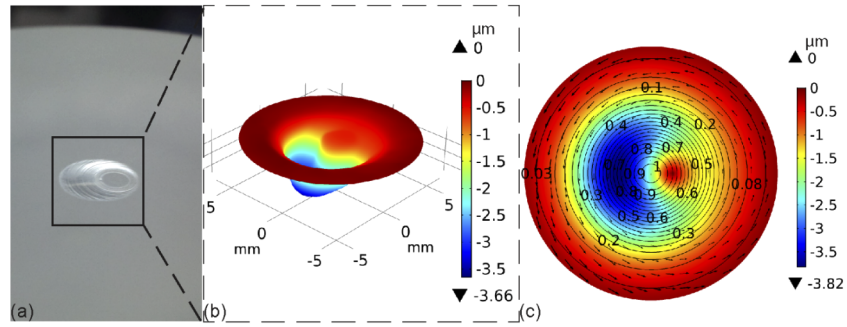


**Fig. 9.** (a) Photographic image of the experimentally polished zone (The circular footprint looks elliptical due to the non-normal view-angle.), (b) measured tool influence function, and (c) simulated tool influence function, pressure contour lines (in bar), and velocity vectors (with tool radius  $R_t = 10$  mm, inclination  $\phi = 5^\circ$ , pressure  $p_o = 1$  bar,  $N_t = 500$  rpm, and  $N_w = 0$  rpm).

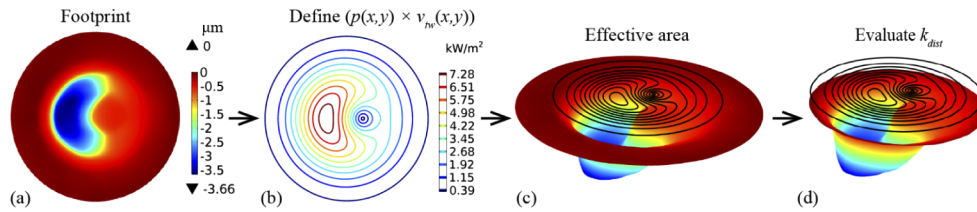


**Fig. 10.** *MRR*-based removal rate data processing steps: (a) acquiring measured footprint, (b) define  $p(x,y) \times v_{nv}(x,y)$  (c) exclude region greater than spot size (i.e.,  $\sqrt{x^2 + y^2} \geq \frac{D}{2}$ ) and (d) evaluate  $k_{dist}$  using effective volume within spot region.

Figure 11 shows the bar chart comparison of mean Preston’s constant evaluated using peak-depth based method ( $k_p$ ), volume-based method ( $k_v$ ) and distributed *MRR*-based method ( $k_{dist}$ ). Each method is evaluated using three different active diameters (i.e.,  $A = 0, 1.743$  and  $3.743$  mm). The standard error is least in distributed *MRR*-based evaluation.

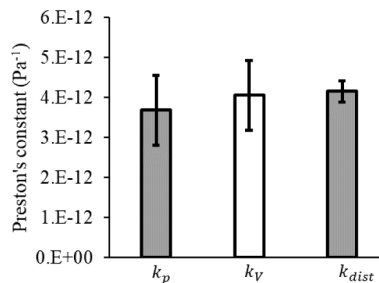


**Fig. 11.** Comparison of Preston’s constant evaluated using peak-depth based ( $k_p$ ), volume-based ( $k_v$ ) and distributed *MRR*-based method ( $k_{dist}$ ). The standard error in Preston’s constant was evaluating using active diameter  $A = 0, 1.743$  and  $3.743$  mm.

#### 4.2. Parametric survey experiment design

The survey experiment space was designed using Taguchi’s L27 orthogonal array method. The optical manufacturing process parameters are active diameter ( $A$ ), feed ( $B$ ), pressure ( $C$ ), spot

size ( $D$ ), and tool speed ( $E$ ). These five parameters are often used in controlling the  $MRR$ , surface errors, processing time, and surface quality. Each parameter is assigned to three levels (Table 2) based on a predetermined machine's dynamic range and the numerical analysis study. During the experiments, the parameter levels were varied according to the design table using the numerically controlled machine tool (MCP 250, OptoTech) described in Section 2.1. Also, the complete combinations of the process parameters used in the experimental design are presented in Table 4.

**Table 2. Three levels assigned to the experimental process parameters**

Level	Active diameter ( $A$ )(mm)	Feed ( $B$ )(mm/min)	Pressure ( $C$ )(bar)	Spot size ( $D$ )(mm)	Tool speed ( $E$ )(rpm)
1	0	0.8	1	3	760
2	1.743	1	1.25	6	780
3	3.743	1.2	1.5	9	800

#### 4.3. Comprehensive experiment procedure

In order to guarantee the full traceability of the presented survey data as a reference, a comprehensive description of the experimental setting is described in detail. The experimental workpiece samples were prepared by grinding and polishing using machine tools MCG 150 and MCP 250 (OptoTech), respectively. During grinding, the best-fit sphere was generated on the blank with a diamond cup wheel tool (mean diameter = 45 mm; radius = 2 mm; grain size = D64). An aspheric surface was then generated using a rough diamond wheel tool (width = 12 mm; radius = 50 mm; grain size = D64) followed by a fine aspheric grinding phase using a diamond wheel tool (width = 12 mm; radius = 50 mm; grain size = D20). Polishing experiments were conducted on an even aspheric surface composed of BK7 optical glass procured from Schott AG (cylindrical blanks diameter = 70 mm; thickness = 20 mm). The following aspheric equation was used for determining feed progression:

$$z = \frac{cy^2}{1 + \sqrt{1 - (1 + K_{\text{conic}})c^2y^2}} + A_4y^4 + A_6y^6 + A_8y^8 + A_{10}y^{10} + A_{12}y^{12}, \quad (19)$$

where the curvature  $c$  is  $(-1/71.42) \text{ mm}^{-1}$ , conic constant  $K_{\text{conic}}$  is 0, and  $A_{\text{even}}$  coefficients are  $A_4 = 0.566322 \times 10^{-6} \text{ mm}^{-3}$ ,  $A_6 = 0.174788 \times 10^{-9} \text{ mm}^{-5}$ ,  $A_8 = -0.218562 \times 10^{-12} \text{ mm}^{-7}$ ,  $A_{10} = 0.19529 \times 10^{-15} \text{ mm}^{-9}$ , and  $A_{12} = -0.70000 \times 10^{-19} \text{ mm}^{-11}$ . The sagittas for the aspherical equation are shown in Table 3.

**Table 3. Sagittas at various radial distances of the aspherical workpiece surface.**

$y$ (mm)	0	4	8	12	16	20	24	28	34
$z$ (mm)	0	-0.11196	-0.44711	-1.00316	-1.77598	-2.75958	-3.94615	-5.32602	-7.73851

The upper layer of the flexible membrane-polishing tool was prepared by pasting a 1-mm-thick and 16-mm-diameter polyurethane pad (GR-35). The polishing tool was dressed using a bonded abrasive tool (ring tool, diameter = 12.5 mm, lip radius = 1 mm, grain size = D64). During the experiment, the wear on the polishing pad in the contact zone of the pad surface was monitored and controlled to minimize practical uncertainties. Figures 12(a) and (b) shows the SEM images of the unused and used polyurethane pad. A fresh polishing pad was used in each trial to limit the variation caused by pad wear or aquaplaning of the pad [26,27]. Tool pad surfaces prior to experiments was dressed using electroplated diamond cup wheel to condition the tool into its geometric shape matching the target radius of curvature and dimensions. During the dressing process, constant feed rate of 0.1 mm/min was given to polishing tool rotating at 400 rpm with

a safety clearance of 0.1 mm from the dressing tool rotating at 600 rpm. Spark out time (time for which axes remains at their positions after reaching the set position on dressing tool) of 60 s was given to improve the final surface quality. We applied the identical dressing process for all polishing pads used in the survey study.

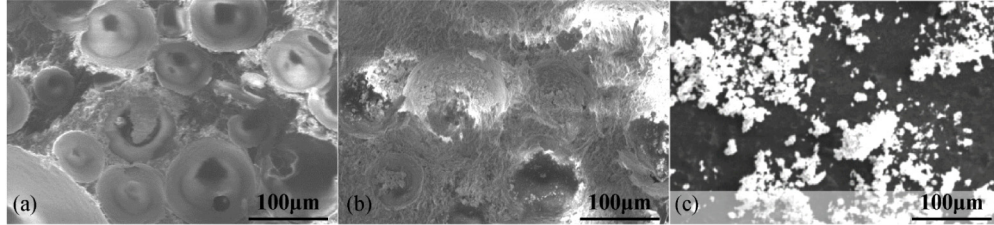


**Fig. 12.** SEM images: (a) polyurethane pad before polishing, (b) polyurethane pad after polishing, and (c) agglomerates of cerium oxide particles.

A suspension of cerium oxide and water was prepared as the polishing compound (concentration = 30 g/L). The cerium oxide used in the slurry (white) had a pH of 7 and particle size ranging from 0.9–1.3  $\mu\text{m}$ . Figure 12(c) shows a scanning electron microscopy (SEM) image of the agglomerates in the polishing compound.

#### 4.4. Experimental data and analysis

Parametric survey analysis was performed using the experimental design presented in Table 2. The distributed *MRR*-based removal rate values are evaluated and presented in Table 4. Also, signal-to-noise (*S/N*) ratios were computed to analyze the *MRR* and identify the most effective process parameters that maximize the *MRR* response.

$$S/N_{mean} = \frac{1}{n} \sum_{i=1}^n (-10 \log_{10}(1/MRR_i^2)), \quad i = 1, 2, \dots, n, \quad (20)$$

where  $MRR_i$  is the *MRR* for the  $i^{\text{th}}$  trial and  $n$  is the total number of trials with the polishing parameter factors.

In order to find the most efficient removal run condition (i.e., highest sensitivity run control parameter), the *S/N* ratio values in Table 4 are averaged for each polishing parameter spaces. The outcome represents the relative response strength of the factors and levels, and the graph in Fig. 13 (left) visualizes the effectiveness of each control parameter on the *S/N* ratio and mean *S/N* ratio. For instance, combination A2B1C2D3E1 provides the highest *S/N* ratio.

The significance of each control parameter was statistically analyzed using analysis of variance for the average *MRR* (Table 5). There were several uncontrolled and unpredictable parameters in the experiments (e.g., distribution of the polishing slurry at the interface, slurry particle size, and height and size of asperities on the polyurethane pad), which may have affected the statistical response data.

The analysis results indicated that the spot size  $D$  was the most significant parameter affecting the response of the experimental removal rate; it contributed 62.17% to the *MRR*, where the *P*-value of spot size indicates a strong significance. The active diameter  $A$  was the second most significant factor, with contributions of 14.98% to the *MRR*. The main effectiveness trends of control parameters for the *MRR* are shown in Fig. 13 (right). The *MRR* increases with an increase in the spot size. However, no such trend was observed for the other factors.

As another insightful bi-product worth to mention, a newly defined Polishing Power,  $P_p$ , over the removal region can be derived from Eq. (18) including the pressure, velocity, contact area and processing time. The terms on the right-hand side of the Eq. (18) can be re-grouped as a

**Table 4. Experimental Survey Data: Material removal rates (MRRs), signal-to-noise (S/N) ratios, polishing interface power, and distributed MRR-based Preston’s constant ( $k_{dist}$ ).**

ID No.	Taguchi’s L27 design code <sup>a</sup>	MRR ( $\text{mm}^3\text{min}^{-1}$ )	S/N ratio	Power $P_p$ (W)	$k_{dist}$ ( $\text{Pa}^{-1}$ )
1	A1B1C1D1E1	0.0326	-29.7397	0.178	$3.06 \times 10^{-12}$
2	A1B1C1D1E2	0.0530	-25.5221	0.178	$4.97 \times 10^{-12}$
3	A1B1C1D1E3	0.0552	-25.1642	0.178	$5.18 \times 10^{-12}$
4	A1B2C2D2E1	0.1424	-16.9290	0.903	$2.63 \times 10^{-12}$
5	A1B2C2D2E2	0.1298	-17.7341	0.903	$2.40 \times 10^{-12}$
6	A1B2C2D2E3	0.1238	-18.1451	0.904	$2.28 \times 10^{-12}$
7	A1B3C3D3E1	0.2594	-11.7207	2.499	$1.73 \times 10^{-12}$
8	A1B3C3D3E2	0.1997	-13.9914	2.501	$1.33 \times 10^{-12}$
9	A1B3C3D3E3	0.1988	-14.0323	2.504	$1.32 \times 10^{-12}$
10	A2B1C2D3E1	0.5104	-5.84100	2.181	$3.90 \times 10^{-12}$
11	A2B1C2D3E2	0.3872	-8.24190	2.186	$2.95 \times 10^{-12}$
12	A2B1C2D3E3	0.5284	-5.54060	2.190	$4.02 \times 10^{-12}$
13	A2B2C3D1E1	0.1027	-19.7679	0.282	$6.07 \times 10^{-12}$
14	A2B2C3D1E2	0.0831	-21.6117	0.283	$4.90 \times 10^{-12}$
15	A2B2C3D1E3	0.0234	-32.6104	0.283	$1.38 \times 10^{-12}$
16	A2B3C1D2E1	0.2014	-13.9167	0.761	$4.41 \times 10^{-12}$
17	A2B3C1D2E2	0.1677	-15.5081	0.762	$3.67 \times 10^{-12}$
18	A2B3C1D2E3	0.2509	-12.0094	0.764	$5.48 \times 10^{-12}$
19	A3B1C3D2E1	0.2053	-13.7532	1.210	$2.83 \times 10^{-12}$
20	A3B1C3D2E2	0.1353	-17.3767	1.214	$1.86 \times 10^{-12}$
21	A3B1C3D2E3	0.2449	-12.2207	1.218	$3.35 \times 10^{-12}$
22	A3B2C1D3E1	0.2849	-10.9051	1.838	$2.58 \times 10^{-12}$
23	A3B2C1D3E2	0.1821	-14.7924	1.844	$1.65 \times 10^{-12}$
24	A3B2C1D3E3	0.2234	-13.0186	1.850	$2.01 \times 10^{-12}$
25	A3B3C2D1E1	0.1054	-19.5405	0.250	$7.02 \times 10^{-12}$
26	A3B3C2D1E2	0.0300	-30.4443	0.251	$1.99 \times 10^{-12}$
27	A3B3C2D1E3	0.0232	-32.6844	0.252	$1.54 \times 10^{-12}$

<sup>a</sup>The code means the experimental parameter values in Table 2. For instance, A2B2C2D2E3 run’s polishing parameters are Active diameter ( $A$ ) = 1.743 mm, Feed ( $B$ ) = 1 mm/min, Pressure ( $C$ ) = 1.25 bar, Spot size ( $D$ ) = 6 mm and Tool speed ( $E$ ) = 800 mm.

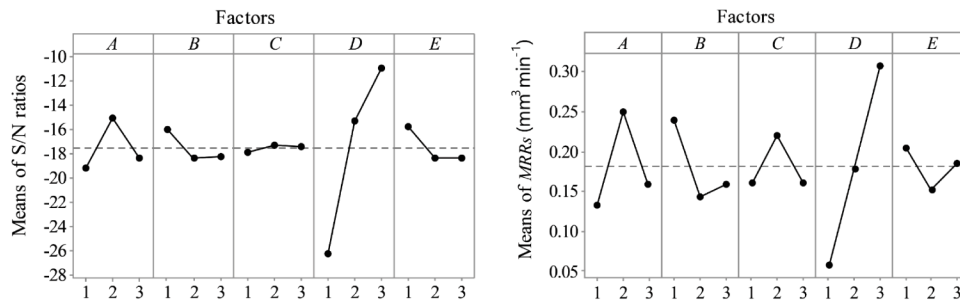


**Fig. 13.** Polishing parameter effectiveness graph in terms of S/N ratio (left) and MRR (right).

**Table 5. Statistical analysis of the MRR variance from the experimental survey result.<sup>a</sup>**

Source	DF	Adj SS	Adj MS	F-Value	P-Value	% Contribution
Active diameter (A)	2	0.06875	0.034373	22.57	0.000	14.98
Feed (B)	2	0.04687	0.023433	15.39	0.000	10.21
Pressure (C)	2	0.02072	0.010359	6.80	0.007	4.51
Spot size (D)	2	0.28533	0.142666	93.67	0.000	62.17
Tool speed (E)	2	0.01295	0.006474	4.25	0.033	2.82
Error	16	0.02437	0.001523			
Total	26	0.45898				
Model Summary						
S		R-sq				
0.0390259		94.69%				

<sup>a</sup>Note: DF is the total degrees of freedom; Adj SS is the adjusted sums of squares; Adj MS is the adjusted mean squares measure; S is the standard deviation; R-sq or R<sup>2</sup> is the percentage of variation in the response.

product of  $k_{dist}$  and  $P_p$ ,

$$MRR = k_{dist} \left( -\frac{P_o}{\tau} \int_0^\tau \left( \iint e^{-\frac{1}{2} \frac{(x-x_c)^2 + (y-y_c)^2}{\sigma^2}} v_{tw}(x, y) dx dy \right) dt \right) = k_{dist} \times P_p, \quad (21)$$

where  $P_p$  is the average polishing power for the processing time  $\tau$ . Thus, the  $P_p$  is evaluated as

$$P_p = \frac{MRR}{k_{dist}} = -\frac{1}{\tau} \int_0^\tau \left( \iint P_o e^{-\frac{1}{2} \frac{(x-x_c)^2 + (y-y_c)^2}{\sigma^2}} v_{tw}(x, y) dx dy \right) dt. \quad (22)$$

Figure 14 plots the scatter  $k_{dist}$  values as a function of average polishing power  $P_p$  (units in watt, W) obtained from the parametric survey listed in Table 4 including all different polishing process parameters.

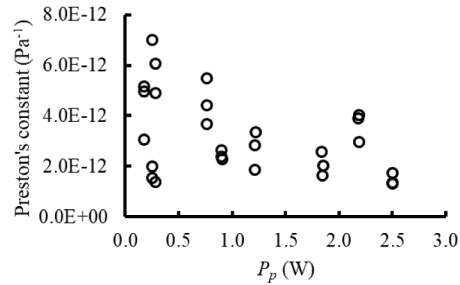


**Fig. 14.** Preston's constant ( $k_{dist}$ ) variation with average polishing power  $P_p$  at tool and workpiece interface.

The scatter plot between Preston's constant and polishing power was obtained from the  $MRR$  and the  $k_{dist}$  as given in Eq. (21) and Eq. (22). Scattered value of Preston's constant is affected by the parameters in the parametric survey study including active diameter, feed, pressure, spot size and tool speed. Here, low  $P_p$  indicate low value of product of the pressure and relative velocity. As shown in Fig. 14, the  $k_{dist}$  scatter is high when a tool operates at low power and the scatter reduces as the power increases. Therefore, it may be inferred that a tool will have lower scatter of Preston's constant at higher polishing power.

This observation-based empirical conclusion is that the scattering is least when polishing tool operates at high polishing power, therefore the predictive simulation modeling may efficiently predict *MRR* and optimize the CCOS runs targeting surface errors if the polishing process parameters are chosen within the high polishing power consumption range.

## 5. Concluding remarks

In this study, we performed an experimental survey and numerical analyses of various computer-controlled optical surfacing process parameters involved in sub-aperture pad polishing of Schott BK7 optical glass. The systematic large survey data with statistical analysis results provided a clear understanding of the changes in the instantaneous *MRR* and Preston's constant behavior during the polishing process. Especially, using the distributed *MRR*-based Preston's constant resulted in improved predictability of the *MRR* and *DRR*.

There are additional parameters to be investigated and explored as an expanded future survey study. For instance, the topography of tool/pad surfaces, slurry distribution as a function of contacting area size, and the ratio between tool size and substrate size, which varies locally for aspheric manufacturing applications, are the remaining parameters beyond the scope of the presented work.

To represent realistic and applied case experiments ensuring that the measured removal rates and the reported parameter range values are still valid for aspheric fabrication processes (i.e., maintaining good and intimate contact between the tool and aspheric substrate), the presented parametric survey study was performed using the aspheric substrate. Most simple experiments performed on a flat or spherical substrate cannot demonstrate this aspect. This is another factor differentiating our contribution compared to the existing literature data.

We acknowledge that the results reported may not be applicable for all types of optical polishing process because the actual polishing process often depends on several complicated factors. However, the experiments were systematically designed to represent a wide variety of cases with widely accepted general process parameters (e.g. active diameter, feed, pressure, spot size, and tool speed). In addition, all the actual experimental parameters are clearly defined, depicted, and described in this paper so the data and results of this survey study can be reproduced for crosschecks.

A stable TIF for accurate removal modeling, control of tool stiffness, and smoothing ability are three important characteristics of sub-aperture polishing tools for deterministically controlling optical surface shape and quality. As the full potential applications of aspheric/free-form surfaces are yet to be identified, there is wide scope for developing polishing and figuring technologies to meet stringent design requirements and tolerances.

## Acknowledgments

The authors acknowledge the Council of Scientific and Industrial Research (CSIR), New Delhi, India, for assistance provided under a CSIR-SRF fellowship and support of their colleagues from CSIR-CSIO, Chandigarh, India who provided the necessary resources, insight, and expertise that greatly assisted the research. This research was also made possible in part by the Technology Research Initiative Fund Optics/Imaging Program at the University of Arizona, USA.

## Disclosures

The authors declare that there are no conflicts of interest.

## References

1. T. I. Suratwala, M. D. Feit, and W. A. Steele, "Toward deterministic material removal and surface figure during fused silica pad polishing," *J. Am. Ceram. Soc.* **93**(5), 1326–1340 (2010).

2. D. W. Kim, S. W. Kim, and J. H. Burge, "Non-sequential optimization technique for a computer controlled optical surfacing process using multiple tool influence functions," *Opt. Express* **17**(24), 21850–21866 (2009).
3. R. A. Jones, "Optimization of computer controlled polishing," *Appl. Opt.* **16**(1), 218–224 (1977).
4. J. B. Johnson, D. W. Kim, R. E. Parks, and J. H. Burge, "New approach for pre-polish grinding with low subsurface damage," in *Optical Manufacturing and Testing IX*, J. H. Burge, O. W. Fahnle, and R. Williamson, eds. 2011 (Spie-Int Soc Optical Engineering).
5. T. Suratwala, R. Steele, M. D. Feit, L. Wong, P. Miller, J. Menapace, and P. Davis, "Effect of rogue particles on the sub-surface damage of fused silica during grinding/polishing," *J. Non-Cryst. Solids* **354**(18), 2023–2037 (2008).
6. R. J. Noll, "Effect of mid- and high-spatial frequencies on optical performance," *Opt. Eng.* **18**(2), 182137 (1979).
7. J. C. Stover, *Optical Scattering: Measurement and Analysis* (SPIE, 1995).
8. J. E. Harvey, N. Choi, A. Krywonos, and J. G. Marcen, "Calculating BRDFs from surface PSDs for moderately rough optical surfaces," *Proc. SPIE* **7426**, 74260I (2009).
9. X. Y. Guo, Y. Shu, G. H. Kim, M. Palmer, H. Choi, and D. W. Kim, "Pseudorandom orbiting stroke for freeform optics postprocessing," *Opt. Eng.* **58**(9), 092608 (2019).
10. J. Lin, C. J. Wang, H. Ye, W. Yang, and Y. B. Guo, "Effect of the tool influence function shape of the semirigid bonnet to the tool path ripple error," *Opt. Eng.* **54**(11), 115104 (2015).
11. D. W. Kim and J. H. Burge, "Rigid conformal polishing tool using non-linear visco-elastic effect," *Opt. Express* **18**(3), 2242–2257 (2010).
12. O. W. Fahnle, H. van Brug, and H. J. Frankena, "Fluid jet polishing of optical surfaces," *Appl. Opt.* **37**(28), 6771–6773 (1998).
13. E. P. Robert, "Specifications: figure and finish are not enough," *Proc. SPIE* **7071**, 70710B (2008).
14. J. Del Hoyo, H. Choi, J. H. Burge, G. H. Kim, and D. W. Kim, "Experimental power spectral density analysis for mid- to high-spatial frequency surface error control," *Appl. Opt.* **56**(18), 5258–5267 (2017).
15. M. J. Cumbo, D. Fairhurst, S. D. Jacobs, and B. E. Puchebner, "Slurry particle size evolution during the polishing of optical glass," *Appl. Opt.* **34**(19), 3743–3755 (1995).
16. H. Lei and J. B. Luo, "CMP of hard disk substrate using a colloidal SiO<sub>2</sub> slurry: preliminary experimental investigation," *Wear* **257**(5-6), 461–470 (2004).
17. J. L. Yuan, P. Zhao, J. Ruan, Z. X. Cao, W. H. Zhao, and T. Xing, "Lapping and polishing process for obtaining super-smooth surfaces of quartz crystal," *J. Mater. Process. Technol.* **138**(1-3), 116–119 (2003).
18. D. Walker, W. Hsing-Yu, G. Yu, H. Li, W. Zhang, and C. Lu, "Insight into aspheric misfit with hard tools: mapping the island of low mid-spatial frequencies," *Appl. Opt.* **56**(36), 9925–9931 (2017).
19. A. Beaucamp and Y. Namba, "Super-smooth finishing of diamond turned hard X-ray molding dies by combined fluid jet and bonnet polishing," *CIRP Ann.* **62**(1), 315–318 (2013).
20. C. Shi, Y. Peng, L. Hou, Z. Wang, and Y. Guo, "Micro-analysis model for material removal mechanisms of bonnet polishing," *Appl. Opt.* **57**(11), 2861–2872 (2018).
21. C. Shi, Y. Peng, L. Hou, Z. Wang, and Y. Guo, "Improved analysis model for material removal mechanisms of bonnet polishing incorporating the pad wear effect," *Appl. Opt.* **57**(25), 7172–7186 (2018).
22. A. G. Lu, K. Guo, T. Jin, and Q. F. Liu, "Modeling and experimentation of dynamic material removal characteristics in dual-axis wheel polishing," *Int. J. Mech. Sci.* **151**, 523–536 (2019).
23. Y. P. Feng and H. B. Cheng, "Calibration method for dual-tilt-axis tool based on image thresholding of skew tool influence function," *Opt. Eng.* **58**(9), 092606 (2019).
24. R. Pan, W. Y. Zhao, B. Zhong, D. J. Chen, Z. Z. Wang, C. Q. Zha, and J. W. Fan, "Evaluation of removal characteristics of bonnet polishing tool using polishing forces collected online," *J. Manuf. Process.* **47**, 393–401 (2019).
25. X. Su, P. Ji, Y. Jin, D. Li, D. Walker, G. Y. Yu, H. Y. Li, and B. Wang, "Simulation and experimental study on form-preserving capability of bonnet polishing for complex freeform surfaces," *Precis. Eng.* **60**, 54–62 (2019).
26. S. L. Wan, X. C. Zhang, W. Wang, and M. Xu, "Effect of pad wear on tool influence function in robotic polishing of large optics," *Int. J. Adv. Manuf. Technol.* **102**(5-8), 2521–2530 (2019).
27. B. Zhong, H. Z. Huang, X. H. Chen, J. Wang, R. Pan, and Z. J. Wen, "Impact of pad conditioning on the bonnet polishing process," *Int. J. Adv. Manuf. Technol.* **98**(1-4), 539–549 (2018).
28. F. Preston, "The theory and design of plate glass polishing machines," *J. Glass Technol.* **11**, 214–256 (1927).
29. G. Marckmann and E. Verron, "Comparison of hyperelastic models for rubber-like materials," *Rubber Chem. Technol.* **79**(5), 835–858 (2006).
30. L. M. Cook, "Chemical processes in glass polishing," *J. Non-Cryst. Solids* **120**(1-3), 152–171 (1990).
31. A. B. Shorey, S. D. Jacobs, W. I. Kordonski, and R. F. Gans, "Experiments and observations regarding the mechanisms of glass removal in magnetorheological finishing," *Appl. Opt.* **40**(1), 20–33 (2001).
32. J. E. DeGroote, A. E. Marino, J. P. Wilson, A. L. Bishop, J. C. Lambropoulos, and S. D. Jacobs, "Removal rate model for magnetorheological finishing of glass," *Appl. Opt.* **46**(32), 7927–7941 (2007).
33. T. Suratwala, W. Steele, L. Wong, M. D. Feit, P. E. Miller, R. Dylla-Spears, N. Shen, and R. Desjardin, "Chemistry and formation of the beilby layer during polishing of fused silica glass," *J. Am. Ceram. Soc.* **98**(8), 2395–2402 (2015).
34. W. L. Zhu and B. Anthony, "Investigation of critical material removal transitions in compliant machining of brittle ceramics," *Mater. Des.* **185**, 108258 (2020).
35. C. Wang, Z. Wang, X. Yang, Z. Sun, Y. Peng, Y. Guo, and Q. Xu, "Modeling of the static tool influence function of bonnet polishing based on FEA," *Int. J. Adv. Manuf. Technol.* **74**(1-4), 341–349 (2014).